Composites Science and Technology 192 (2020) 108124

Contents lists available at ScienceDirect

Composites Science and Technology

journal homepage: http://www.elsevier.com/locate/compscitech

Interface binding and mechanical properties of MXene-epoxy nanocomposites

Yelena Sliozberg [a,*], Jan Andzelm [a], Christine B. Hatter [b], Babak Anasori [c], Yury Gogotsi [b], Asha Hall [a]

[a] U.S. Army Combat Capabilities Development Command Army Research Laboratory, Aberdeen Proving Ground, MD, 21005-5069, USA
[b] A.J. Drexel Nanomaterials Institute and Department of Materials Science and Engineering, Drexel University, 3141 Chestnut St., Philadelphia, PA, 19104, USA
[c] Integrated Nanosystems Development Institute and Department of Mechanical and Energy Engineering, Indiana University-Purdue University Indianapolis, Indianapolis, IN, 46202, USA

A B S T R A C T

Thermosetting epoxy polymers exhibit excellent stiffness and strength and are commonly utilized as matrices to make fiber reinforced composites. However, epoxy thermosets are brittle and typically possess a low fracture toughness that restricts their applications. One promising mechanism for improving mechanical properties of epoxy is the integration of micro- and nano-scale fillers. MXenes, a large family of 2D transition-metal carbides, carbonitrides, and nitrides, can be used to produce multifunctional polymer nanocomposites due to their excellent electrical, thermal, and mechanical properties. We employed density functional theory and coarse-grained molecular dynamics simulations to evaluate binding energy and microscopic mechanisms of fracture under uniaxial tension for MXene-epoxy composites. The simulation results were verified by manufacturing $Ti_3C_2T_x$ MXene-epoxy composites and studying their structure and fracture surfaces. MXene-epoxy binding energies are largely unaffected by MXene type (Ti_2CT_x or $Ti_3C_2T_x$). Binding between $Ti_3C_2T_x$ and epoxy becomes stronger with less hydrogen coverage of $Ti_3C_2T_x$ surface due to increase in favorable electrostatic interactions. The Young's modulus of MXene-epoxy composites is greater compared to the neat epoxy which originates from stress transfer between the matrix and the nanofiller, the modulus linearly increases with the filler loading up to 1 vol %. At higher filler contents, the increase of the modulus is reduced due to filler aggregation. Void formation was detected near edges of the particles in MXene-epoxy composites under deformation from both experimental and simulation studies of the fracture surfaces. From these observations, we expect the MXene fillers to improve epoxy toughness and enhance its mechanical performance.

1. Introduction

Carbon fiber and glass fiber reinforced polymer composite materials are used in numerous applications that require high stiffness and high strength-to-weight ratios. Polymer matrix materials chosen for these composites are often thermosetting polymers, which have many valuable properties required for structural applications, such as excellent stiffness and strength, reduced shrinkage, high adhesive strength, chemical and heat resistance, environmental stability, and relatively low cost, but they are brittle and typically possess low fracture toughness which restricts their applications [1]. Recent works have demonstrated that the mechanical properties of thermoset resins can be improved by an integration of micro- and nanofillers and their results have been summarized in numerous papers [2–7] and reviews [1,8–11]. Nanocomposites have enhanced mechanical properties compared to traditional composites due to the stress transfer between the matrix system and the nanofiller which serves as the second phase [1,11], matrix-nanofiller interfacial debonding leading to the local plastic deformation [1,3] and increased volume of interphase due to small size and large specific surface area of nanoparticles [1].

MXenes, a family of 2D transition-metal carbides, carbonitrides, and nitrides discovered at Drexel University in 2011, can be used to produce multifunctional polymer nanocomposites due to their excellent electrical, thermal, and mechanical properties as well as 2D morphology [12]. Recent research in MXene-polymer composites has shown self-healing capabilities [13], high thermal conductivity [14], and metallic electrical conductivity [15,16] as well as structural improvement of the epoxy matrix [17]. MXene structure and properties have been summarized in several recent reviews [18–20] and articles [21,22]. MXenes are produced through selective etching of bulk ternary carbide MAX phase precursors [23] and can be delaminated into single and few-layer nanosheets through additional processing. MXenes have a chemical formula of $M_{n+1}X_nT_x$, where M is an early transition metal (e.g., Ti, Mo, V), X is carbon and/or nitrogen, T_x are surface functional groups, and $n = 1–3$ [18,21,24]. The aqueous medium during synthesis produces surface moieties (T_x) such as = O, –OH, and –F creating

* Corresponding author.
E-mail address: yelena.r.sliozberg.civ@mail.mil (Y. Sliozberg).

https://doi.org/10.1016/j.compscitech.2020.108124
Received 25 September 2019; Received in revised form 28 January 2020; Accepted 11 March 2020
Available online 16 March 2020
0266-3538/Published by Elsevier Ltd.

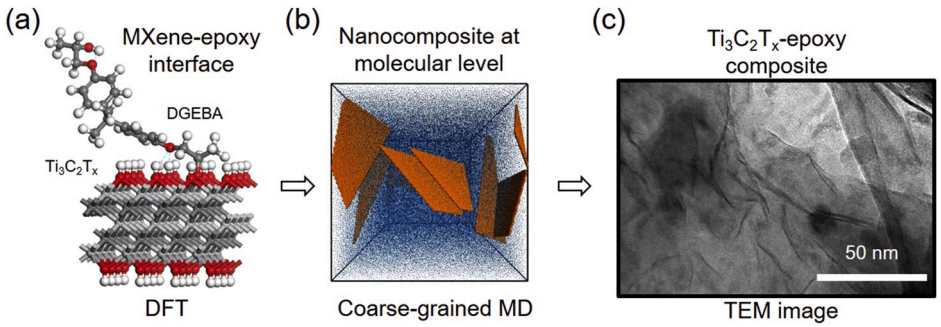

Fig. 1. Schematic overview of the multiscale modeling approach of MXene-epoxy composites by combining DFT and coarse-grained MD simulations. (a) Representative snapshot of DFT simulation of $Ti_3C_2T_x$-DGEBA interface, (b) representative snapshot from coarse-grained MD simulation, (c) TEM images of $Ti_3C_2T_x$-epoxy nanocomposite.

hydrophilic 2D flakes that can be easily dispersed in water and other organic solvents [25,26]. While there are many experimentally synthesized and theoretically predicted MXenes, titanium carbide based MXenes ($Ti_{n+1}C_nT_x$) are most widely studied [18]. Functionalized surface permits MXenes to create covalent bonds with polymer matrix to ensure strong interfacial adhesion and good stress transfer across the interface [14,17]. Few studies have investigated mechanical improvement of epoxy composites using MXenes and show significant improvement of the mechanical properties [17,27,28].

Even though graphene has the highest Young's modulus of 1 TPa among known materials, lack of surface terminations limits use of pristine graphene in epoxy composites. Instead, several types of graphene oxide derivatives have been integrated into epoxy, which show better solubility in the epoxy networks and result in enhanced properties. Although the effective Young's modulus of a single layer of $Ti_3C_2T_x$ is 0.33 ± 0.03 TPa and it is lower than the Young's modulus of graphene, it surpasses the graphene oxide (the Young's modulus is ~0.2 TPa). Additionally, the effective bending rigidity for $Ti_3C_2T_x$ significantly exceeds the bending rigidity of graphene due to the fact that MXene monolayers are ~3 times thicker compared to graphene [35,48]. From these considerations, we expect MXenes to be promising reinforcement candidates as the fillers in epoxy composites.

In addition to experimental research, many computational studies from first principals based on density functional theory (DFT) [22,29–34] and molecular dynamics (MD) [35,36] have provided valuable insight into the structural, thermodynamic, elastic and electronic properties of MXenes. In this work, we focus on prediction of 1) the structural properties of Ti_2CT_x and $Ti_3C_2T_x$ MXenes and diglycidyl ether of bisphenol A (DGEBA) resin interface and 2) clarification of mechanisms of fracture on the molecular level of the nanocomposite under uniaxial tension. Here we employed a multiscale modeling approach by combining two methods: DFT and coarse-grained model of MD simulations to probe interfacial bonding of MXene and mechanism of failure, respectively (Fig. 1). Although, the accuracy of our results is subject to the length and time scales limitations of simulations, the results of this study show microscale mechanisms of MXene-epoxy mechanical improvement in isolation of macroscale factors. Computational results are compared with experimental findings on $Ti_3C_2T_x$-epoxy nanocomposites.

2. Model and methods

2.1. DFT simulations of MXene-epoxy surface

For this study, quantum mechanical simulations employing DFT was used to predict the structural and electronic properties of the MXene-epoxy interface from the first principles. DFT was performed using the Perdew–Burke–Ernzerhof (PBE) exchange correlation functional approximation. All calculations were performed with the DMol3 program as implemented in the Materials Studio suite of modeling programs [37–40]. For quantitative descriptions of charge distributions $Ti_3C_2T_x$-DGEBA systems, the bound compound was divided into atomic fragments and Hirshfeld charges were calculated [41]. The detail description of preparation of molecular models of MXene-epoxy surfaces is presented in Supporting Information 1.1.

2.2. Coarse-grained MD simulations of polymer network

Coarse-grained MD simulations of polymer networks and composites were performed using the standard bead-spring "Kremer-Grest" model [42], which has proven to be a great technique to study microscopic structural and mechanical properties of a broad range of polymer materials, including polymer nanocomposites [43,44] and highly cross-linked polymer networks [45,46].

The model system of the nanocomposite for coarse-grained MD are made from two types of constituents, 1) three-dimensional highly cross-linked polymer network and 2) two-dimensional filler sheets. The polymer network and filler are discretized using coarse-grained particles, where polymer particles are bonded to each other with massless springs.

All quantities are expressed in terms of the mass m, the inter-monomer binding energy U_0, the monomer diameter a, and characteristic time $t_{LJ} = \sqrt{ma^2/U_0}$. Here, DGEBA epoxy network cured with tetrafunctional diamine is approximated as repeat units connected with the virtual bonds of 9.5 Å length and bond angle of 110° [47]. Since the bond length in our model is approximately $0.9655a$, the model length scale $a \approx 1$ nm and if U_0 is taken to be approximately 300 k_B, then units of pressure, P of U_0/a^3 corresponds to approximately 4.5 MPa.

This modeling system includes several filler nanoflakes made from a single layer of particles in hexagonal lattice, mimicking a hexagonal basal plane of single-layer 2D MXene nanosheet with a thickness of ~0.98 nm [48]. Since bending rigidity of Ti_3C_2 MXenes much higher than other 2D materials [35], each flake is treated as an independent rigid body [49], so the set of particles composing the flake moves and rotates as a single entity. All simulations were executed using LAMMPS [50]. The detail simulation description of preparation of polymer composite is presented in Supporting Information 1.2.

In this study, two cases were considered to determine the relationship between mechanical properties and interfacial properties; 1) all filler particles are allowed to react with polymer and 2) only 10% of the filler particles are reactive. The outcome of this study identified "high coverage" and "low coverage" of reactive terminal groups on the filler surface. Additionally, samples were generated where there were no covalent bonds created between a filler and polymer (referred as "no covalent bond" systems) and the filler sheets have larger lateral size ("large flake" systems). A model of the filler surface with 90–100% nonreactive particles represent weak bonding between MXene and epoxy if there only negligible amount of terminal groups reacts with

epoxy.

In this work, we considered polymer composite systems with the filler volume fractions, ϕ_f, ranging from 0 to 0.013 (which corresponds to 0–5 wt%). Pure polymer highly cross-linked network without the filler was also studied as reference system. Refer to Table S1 in Supporting Information for details of the considered composites in MD simulations.

3. Experimental

3.1. Materials

Epoxy resin used in this study was commercially available diglysidyl ether of bisphenol A (DGEBA) (Epon 828, Hexion). The amine-based curing agent was 4,4′Methylenebis(cyclohexylamine) (PACM, Sigma Aldrich). Ti_3AlC_2 (Carbon-Ukraine) with mesh size $\leq$ 45 μm was used as the MAX phase precursor for MXene synthesis.

3.2. Synthesis of $Ti_3C_2T_x$ MXene

$Ti_3C_2T_x$ MXene was prepared using previously documented HCl–LiF etching methods [51]. Two grams of LiF were added to 20 mL of 9M HCl and mixed using a magnetic stir bar for 5 m until completely dissolved. Then two grams of Ti_3AlC_2 MAX phase was slowly added to the mixture and allowed to stir at 35 °C for 24 h. Resultant mixture was split into two centrifuge tubes and combined with deionized (DI) and then centrifuged for 3 m at 3500 rpm. Afterwards, the supernatant was decanted and remaining sediment was redispersed in DI water and centrifugation was repeated. This washing process was repeated up to 6 times until a pH of 7 was obtained. After the final washing cycle, the multilayer sediment was collected and dried overnight in vacuum oven at 100 °C to remove excess water and powders were collected. Multilayered MXene was then annealed at 500 °C for 1 h in tube furnace under argon flow to prepare MXene powder with oxygen-rich surface functional groups. The previous research showed that $Ti_3C_2T_x$ does not degrade and remains stable upwards of 850 °C. Since our annealing treatment is at a lower temperature (500 °C), the $Ti_3C_2T_x$ structure remain the same and only changes in surface functional groups [51]. Our prior studies on annealing of $Ti_3C_2T_x$ have confirmed that only oxygen functional groups remain on MXene surface at temperatures at 500 °C [52,53].

3.3. Preparation of MXene-epoxy composites

Appropriate amounts of annealed multilayered $Ti_3C_2T_x$ MXene powder were added to epoxy resin that was heated in an oil bath at 80 °C and stirred for 1 h. Mixture was then bath sonicated for 1 h followed by addition of PACM hardener. The composite mixtures were then placed in a speed mixer (ARE-250, Thinky) at 2000 rpm for 10 m. Mixture was then poured into a mold and cured at 70 °C for 4 h followed by post-curing at 160 °C for 2 h. As a control, non-annealed multilayer MXene powders were also used to assess the influence of oxygen-rich functional groups on interactions between epoxy and MXene flakes.

3.4. Characterization of MXene-epoxy composites

Structure and morphology of MXene-epoxy samples were investigated using transmission electron microscopy (TEM, JEOL-2100, Japan) at 200 kV acceleration voltage. Composite samples were mounted in commercial resin and cured followed by ultramicrotomy for cross-section analysis in TEM. Composites fracture surface was investigated using scanning electron microscopy (SEM, Zeiss Supra 50VP, Germany).

4. Results and discussion

4.1. MXene-epoxy binding energy and electrostatic interactions with DFT calculations

DFT calculations were used to evaluate the binding energy and electronic properties of the MXene-epoxy nanocomposites. Initially, we examined the difference in binding energy and C–O bond distance for the different types of MXene-epoxy compounds, namely $Ti_2C(OH)_2$ and $Ti_3C_2(OH)_2$. The assumption for this model was to have the adsorption of one molecule of the lowest energy conformer of DGEBA on a well separated slab of a single layer of MXene.

Our results show that the binding energies of $Ti_2C(OH)_2$-DGEBA and $Ti_3C_2(OH)_2$-DGEBA are −23.4 kcal/mol and −21.4 kcal/mol, respectively. The distance of C–O MXene-epoxy covalent bond is 1.43 Å and 1.44 Å for $Ti_2C(OH)_2$-DGEBA and $Ti_3C_2(OH)_2$-DGEBA, respectively, which is in a range for paraffinic C–O bonds. The structure of bound epoxy largely unaffected by the surface and is close to gas phase, where the similarity with the gas phase is 0.98. We also found that some hydrogen bonds are present in epoxy-MXene and within epoxy. Thus, results suggest that the binding energy of epoxy does not significantly depend on the type of MXene and bonding is well localized to the surface.

The surface environment around the MXene-DGEBA covalent bond was studied as a function of various terminal groups. The binding energies for three following cases were calculated: 1) all terminal groups are –OH (15 –OH groups), 2) there are 7 –OH and 8 = O terminal groups, and 3) all terminal groups there are = O groups (15 = O groups). The binding energy values were computed using two models. The first model includes DGEBA molecule bound to a surface of a single layer of $Ti_3C_2T_x$ with various terminal group coverage and the other surface has only –OH terminal groups, see Fig. 1 (a). The second model considers two DGEBA molecules bound to two surfaces with variable coverage by the functional groups and separated by a T_3C_2 layer. For example, Fig. S1 in Supporting Information shows two bound DGEBA at $Ti_3C_2T_x$ surfaces. Next, we evaluate atomic Hirshfeld charges for $Ti_3C_2T_x$-DGEBA complexes. To facilitate discussion of charge distribution, the sum of the Hirshfeld charges for terminal groups (-OH or = O), named surface1 and surface2, Ti_3C_2 layer and bound DGEBA are presented in Supporting Information Table S2.

$Ti_3C_2(OH)_2$, which surface1 (or surface2) is terminated with only –OH groups, is negatively charged. Our results show that $Ti_3C_2(OH)_2$ surface has the Hirshfeld charge equal to −1.89 in average. When one or two molecules DGEBA bind to the surface of $Ti_3C_2(OH)_2$, we did not observe any significant change of the surface charge, where the charge becomes −1.84 or −1.85 with respect of a number of DGEBA molecules adsorbed (see Table S2). Since the bound DGEBAs have a small negative charge (−0.21 or −0.17), it leads to the electrostatic repulsion between DGEBA and the surface1 or surface2. Although DGEBA forms hydrogen bonds with –OH groups of $Ti_3C_2(OH)_2$ surface, the binding energy is relatively small as it is equal to −21.4 and −23.0 kcal/mol with respect of the number of bound DGEBAs. Charge of the surface without bonded epoxy does not show any strong dependency of the reactive surface termination.

The simulation demonstrates that converting –OH groups to = O groups around the binding site leads to an increase of the negative charge at the surface and positive charge at DGEBA. Subsequently, it leads to increase in favorable electrostatic interactions between $Ti_3C_2T_x$ surface and DGEBA and results in an increase of the binding energy. The most electrostatically favorable interactions are observed for $Ti_3C_2(O)_2$, where the charges on the surface/DGEBA becomes −4.25/0.45 and −4.04/0.43 for one and two bound DGEBA molecules, respectively.

This increase in electrostatic interactions between MXene surface and DGEBA results in significant rise of the binding energy with decrease of –OH terminal groups and increase of = O groups coverage. Interestingly, it happens even with lack of hydrogen bonding between DGEBA

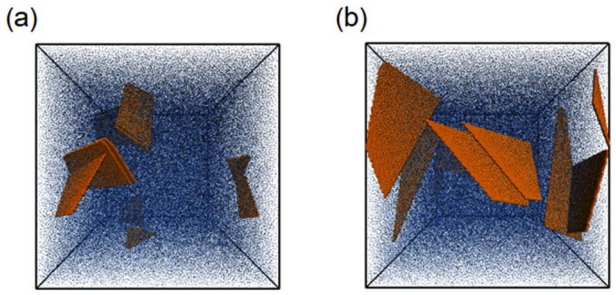

Fig. 2. Representative snapshots from composite simulation of 5 wt% filler at $t = 5{\cdot}10^5 t_{LJ}$, where the flakes size is (a) 23 × 32 a^2, (b) 42 × 61.5 a^2. The polymer network and filler flakes are shown with blue and orange color, respectively.

and MXene modified surface. Compared with −21.4 kcal/mol and −23.0 kcal/mol for the $Ti_3C_2(OH)_2$ binding surface, the binding energy becomes −76.9 kcal/mol and −62.4 kcal/mol for $Ti_3C_2(O)_2$ with one and two bound DGEBA molecules, respectively. Consequently, our results predict that the strongest binding occur between epoxy and MXene if the coverage of –OH terminal groups are low. The binding energies are calculated with respect to the one DGEBA molecule; therefore the total binding energy is −124.8 kcal/mol indicating propensity of DGEBA molecules for binding to two surfaces of MXene 2D particle.

4.2. Structure of MXene-epoxy composites from coarse-grained MD simulations

The detailed microstructures of the equilibrated simulation systems were examined before curing to verify filler aggregation. For this, any flakes located at the distance from each other less than cutoff radius 2.5a are considered to be part of one cluster. Results indicated that rigid filler particles tend to restack in the parallel fashion and aggregate for the higher concentrations as shown in Fig. 2.

The restacking and aggregation already take place for the smaller flakes (23 × 32a^2) at $\phi_f > 0.0025$ (1 wt%) loading of the filler. In general, the size of aggregates made of the filler flakes increases with the loading of the filler, refer to Fig. S2 (a), while at $\phi_f > 0.0076$ (3 wt%), all flakes are incorporated in aggregated clusters (Fig. S2(b)). Interesting, that nanocomposite systems made of epoxy and filler flakes with larger lateral size (42 × 61.5 a^2) show less aggregation compared to the system with the shorter flakes with the same filler volume fraction. Subsequently, epoxy precursor molecules were intercalated between MXene layers leading to an increase in the layer spacing. We discuss the polymer composite structures on the molecular level in detail in Supporting Information 1.4.

Although all interactions used in this simulation study are equally attractive, van der Waals forces between nanofiller flakes become significant due to the large surface area per unit mass and lead to aggregation of the flakes. Parallel orientation of the filler flakes at the distance greater than van der Waals radius has entropic nature. The rigid particle structural organization leads to a rise of free volume and consequently the conformational entropy of the polymer, despite the fact the orientation of the filler decreases their translational entropy. This effect was observed in experimental [54] and theoretical studies [55].

Since it has been shown that the –OH termination is a relatively minor component on MXene surface (around 10%) and mostly = O and –F groups are present [25], we consider that the chemical bonds between filler and polymer have the strength comparable to matrix bonds, as it has been shown by DFT calculations for the smaller amount of –OH terminal groups. Future experimental investigations are necessary to confirm the different effects of –OH and = O groups on mechanical properties.

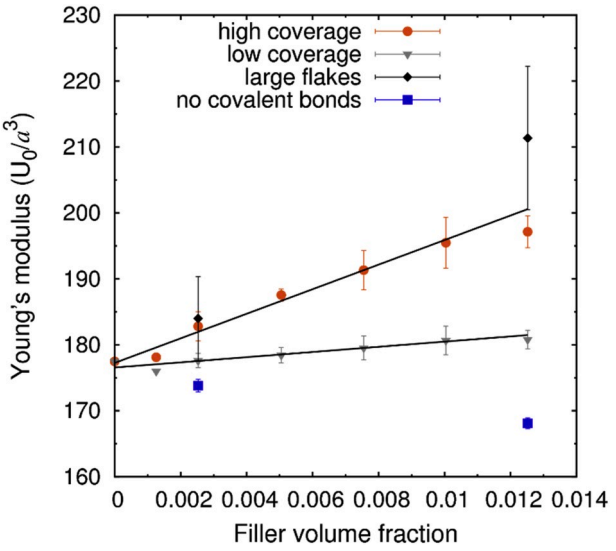

Fig. 3. Calculated Young's modulus as a function of the filler loading for MXene-epoxy composites. Lines connecting the points show the linear prediction from Eq. (1).

4.3. Prediction of mechanical properties improvement from coarse-grained MD simulations: Young's modulus

In Fig. S4 in Supporting Information we show an example of stress-strain curves for the high- and low-coverage systems under the tension for the x direction. Since the nanocomposites are locally anisotropic, the tensile curves differ in different directions. However, all curves show the brittle fracture behavior typical for highly cross-linked networks. In general, a relative Young's modulus increase and strain at break decrease with nanofiller loading as typically observed for epoxy nanocomposites [8]. Fig. 3 shows the Young's modulus for the composites where the modulus was computed as a slope for the Hookean response of stress-strain behavior at the low strain.

The improvement of modulus of the nanocomposites is credited to the filler higher modulus compared to polymer matrix. At the low content of the filler, the reinforcement of the Young's modulus could be estimated from the modified rule of mixture [56].

$$E_c = E_f \eta_0 \eta_1 \phi_f + E_m(1 - \phi_m), \tag{1}$$

where E_f and E_m are the moduli of the filler and matrix, respectively, and ϕ_f and ϕ_m are the volume fractions of the filler and the matrix, respectively. Krenchel orientation factor, η_0 depends on the average orientation of the filler with respect to the applied stress, and $\eta_0 = 8/15$ for randomly oriented 2D filler [56]. The length distribution factor, η_1, takes values between 0 and 1 depending on stress transfer on interfaces and size of the flakes [56]. After fitting the Young's modulus we found that the effective moduli of the filler flake, $E_{eff} = E_f \eta_0 \eta_1$ are equal to 2040 and 570 U_0/a^3 for the high and low interface coverage, respectively. In this model, MXene particles are approximated as rigid bodies, with infinite Young's modulus (having zero strain regardless of applied stress). Therefore, the effective modulus of the flake has a finite value because of the short size of the flake (~32 × 23 nm in the physical units for the small flakes). Since the Young's modulus of the neat cross-linked polymer is 177 U_0/a^3, the flake modulus is ~10 times greater than the modulus of the matrix.

Given that the experimental value of the Young's moduli of a single layer of $Ti_3C_2T_x$ MXene and epoxy resin are equal to 0.33 TPa [48] and 2.5 GPa [3], respectively, we could estimate from eq. 4the maximum E_{eff} of $Ti_3C_2T_x$ MXene to be ~70 times larger than the epoxy modulus. That is possible if the MXene is randomly distributed ($\eta_0 \approx 0.53$) and stress

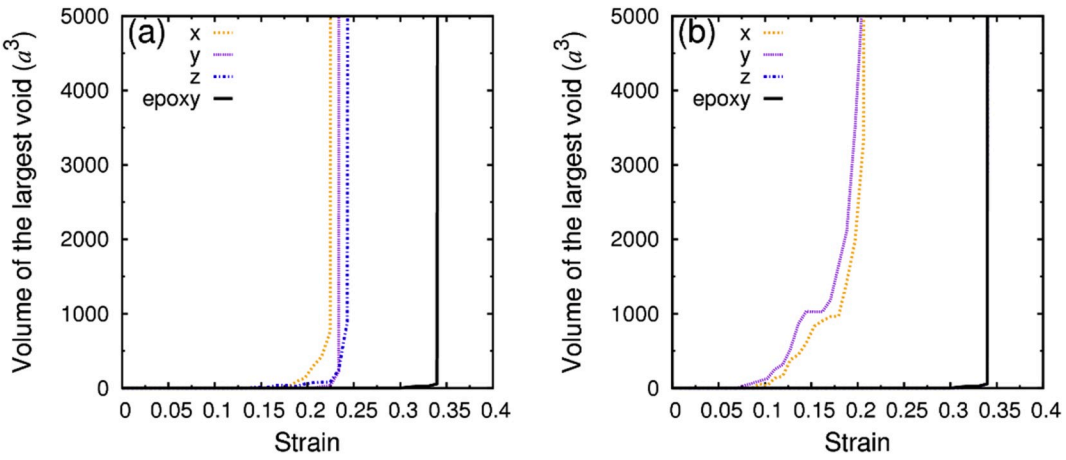

Fig. 4. Volume of the largest void for the nanocomposites with $\phi_f = 0.0025$ (1 wt% filler loading) as a function of the engineering strain during the tensile deformation in x, y and z-directions for MXene-epoxy nanocomposites with a) high surface coverage, (b) for the weak interface model.

transfer is perfect from sufficient covalent bonding at the interface and the filler flakes are large ($\eta_1 \approx 1$). Taking this into account, we could expect the increase of the Young modulus around 16% for only 1 wt% ($\phi_f = 0.0025$) of $Ti_3C_2T_x$. The particle-based molecular dynamics method used in this paper does not allow for performing simulations with very large filler sheets due to current computational limitations. For example, the aspect ratio of simulation filler flakes is 27.5 or size is $23 \times 32\ nm^2$, while the experimental studies use much larger flakes with lateral sizes reaching over 2 μm [15]. That is why we observed only a modest increase of the Young modulus, for example, 3% modulus increase for $\phi_f = 0.0025$ that corresponds to 1 wt% of MXene. The importance of flakes with higher aspect ratio for the successful polymer reinforcement has been shown experimentally. For instance, very little reinforcement is only obtained for polymer-graphene composites with small flakes (aspect ratio of 1000), while both, modulus and strength, were found close to the theoretical limit for flakes with the aspect ratio of 2000 [57]. In agreement with the theoretical and experimental results, our simulation suggest that the increase of the lateral size (aspect ratio) of the filler sheets improves the reinforcement. For example, if filler size was doubled from $23 \times 32\ nm^2$ to $42 \times 61.5\ nm^2$, then the modulus increase for MXene-epoxy composites compared to neat thermoset was 4% and 19% for ϕ_f equal to 0.0025 and 0.0125 (~1 and 5 wt %), respectively, while the increase was 3% and 11% for smaller flakes ($23 \times 32\ nm^2$), as shown on Fig. 3.

Results shown in Fig. 3 suggest that modulus growth slows down at ϕ_f greater than 0.0125 (4 wt%), which is consequence from the aggregation of the filler, that we observed in the simulations. The similar results where shown experimentally, where the storage modulus increase is reduced even for MXene loading greater than 1.0 wt% [17].

Additionally, this simulation demonstrates the importance of stress transfer between matrix and filler material to observe the modulus increase. For example, we observed much less modulus increase for the low coverage model, while the modulus even decreases for model without the chemical bonds compared to the neat epoxy system, as shown in Fig. 3. In this case, the filler acts as a void defect in the material, instead of a reinforcement.

Although, we observed the modulus increase in all the simulated nanocomposites compared to the neat epoxy, with exception of composites without covalent bonding at the interface, the ultimate strain and subsequently the ultimate stress and toughness are generally reduced for the composites for both high and low surface coverage. That outcome stems from a local stress concentration at the composite interface. The analysis of ultimate stress, ultimate strain and toughness is placed in Supporting Information Section 1.5 and Fig. S5.

Nevertheless, such lack of improvement of the ultimate stress and toughness could be consequences of two main limitations of particle-based simulations: short length- and time scales. First, we employed significantly smaller size of filler flakes than the sizes typically used in experimental studies and as a result the effective Young modulus is considerably smaller than expected for the particles with larger lateral size. Moreover, small flakes limit the possibility to observe larger scale phenomena responsible for toughness improvement, such as the crack pinning and crack deflection. Second, the simulated deformation strain rates are extensively greater than experimental rates and model systems could have less time to dissipate energy by filler-polymer surface debonding. In our simulation, we observed the debonding and void formation for the nanocomposites which could be prerequisite for the toughening at the larger scale. We will discuss these events in detail in Section 4.4.

4.4. Bond breaking and void formation

Here, three models are compared: neat highly cross-linked polymer network, 1 wt% $Ti_3C_2T_x$ nanocomposite with high MXene surface coverage of terminal groups, and 1 wt% $Ti_3C_2T_x$ nanocomposite with attractive interface but lacking covalent bonds (weak bonding). The model with the low coverage of reactive terminal groups performs very similar, mechanically, to the model without covalent bonds. Since a model of a single sheet of MXene was used, it is evident that fewer covalent bonds are present on edges of multilayer flakes due to geometrical considerations. This could imply the system would fracture closer to edges of the filler particles if the interface contains covalent bonds (strong interface). We present the bond breaking at the interface in Supporting Information 1.6.

It is predicted that if the stress transfer to the filler central length is elastic, debonding would happen in regions near the filler edges and the plastic nanovoid growth is expected [58]. Rigid nanoparticles, dispersed in the polymer matrix, behave as stress concentration regions during the deformation, so the plastic deformation reduces the constraint around the nanoparticle and is responsible for most of the energy absorption [59]. Here, only single-layer filler flakes are considered and no other type of energy dissipation stemmed from the filler layer separation is included.

In this study, nano-size voids were observed during the tensile deformation. Fig. 4 illustrates the void growth during the tensile deformation, where a volume of the largest void is plotted as a function of the strain.

When the volume of the void starts to increase steeply with the tension, the system undergoes fracture. Our results demonstrate the nanocomposite model with high surface coverage of terminal groups (strong interface) shows the void formation and growth before the

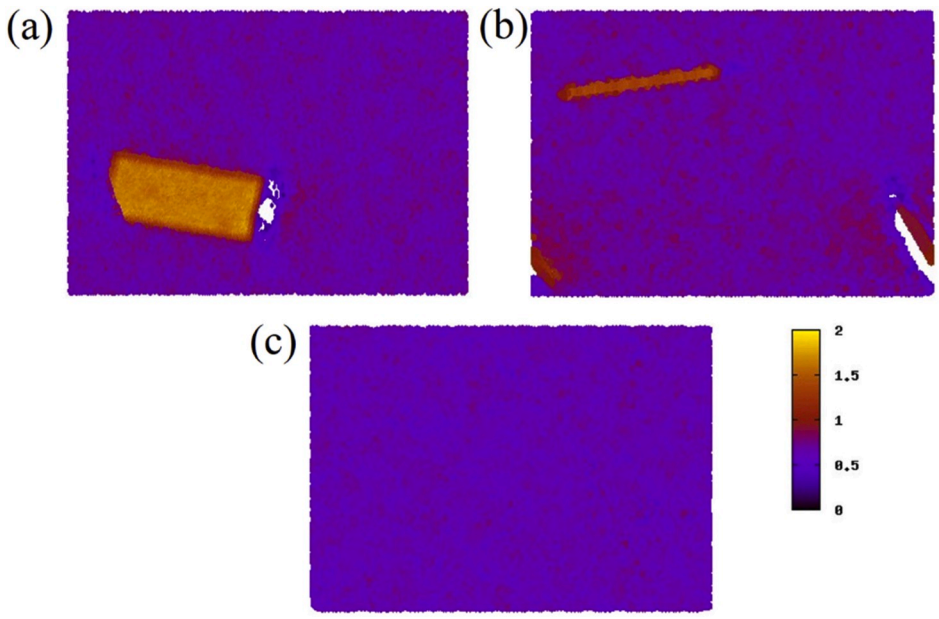

Fig. 5. Representative snapshots taken from tensile deformation in x-direction for models with (a) high surface coverage at $\varepsilon = 0.22$, (b) no covalent bonds on the surface at $\varepsilon = 0.21$, (c) neat polymer network at $\varepsilon = 0.34$. Figures represent 10a slice of the actual simulation box. The color scheme represents the specimen local density.

fracture as shown in Fig. 4 (a). Pure polymer network does not produce voids and fractured abruptly as the high crosslink density of pure polymer network constrained void growth. The rate of the volume growth is significantly higher and the free volume begins to increase at the lower strains for the weak interface model of nanocomposites under the tension in x and y direction compared to the high surface model. Moreover, the weak interface model starts to form void in x and z direction deformation at lower strain compared with both high surface coverage and neat polymer network. The behavior of the weak interface model under tension in z-direction is near identical to the pure polymer network, where the system fractured without void formation, which illustrates significance of orientation for the weak interface model. The directionality of the tension is less important for the strong interface model because flakes are connected with the matrix and consequently stress transfer between matrix and flakes occurs.

Finally, a location of the voids with respect of the basal plane and edges of the filler flakes, was investigated. As expected, results show that voids are always initiated near the edges of the flakes (a void border is less than 5a from any filler particle) for the nanocomposite model with high surface coverage, where the average distance from the filler edge to the void boundary is 2.23a (~2 nm). In this case, the voids form as the results of bond breaking at the interface and the polymer matrix close to the filler edges. In contrast, for weak interface model of nanocomposite under tension in x and y directions, the voids are originated at the basal plane surface of the filler, before the polymer matrix bonds begin to break. An exception is the tension in z-direction, where the nanocomposite with the weak interface fractured without void formation.

Fig. 5 shows the examples of these voids formed under the tensile deformations for our model systems. The strong interface model (Fig. 5 (a)) has a void formed near the filler edge similar to the experimental results. The weak interface model shown in Fig. 5 (b) demonstrates void creation around the filler, while the pure epoxy does not have any voids.

Thus, simulation results show that the nanocomposites with strong interface undergo void formation near the edge of the filler in agreement with the experimental observations of $Ti_3C_2T_x$–epoxy fracture surfaces as shown in Section 4.2 (Fig. 7). In contrast, the nanocomposite with the weak interface fails by adhesive fracture at the basal plane of the flakes, which was not seen in the experimental images. An exception is a case when the tension direction is normal to the edges of the filler flake as we observed for tension in z-direction for the weak interface model.

The plastic nanovoid growth is expected to delay material fracture by dissipation of fracture energy and subsequently improvement of fracture toughness [1]. Although we observed the formation of voids, no increase in toughness was observed for the nanocomposites. This contradiction can be explained by the fact that the simulation strain rates are several orders of magnitude greater than experimental rates and thus the voids in the simulated nanocomposites have not enough time to grow and subsequently dissipate energy. For instance, the maximum void size for

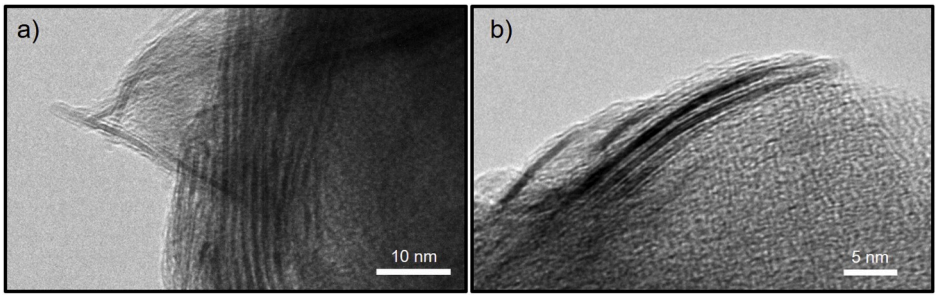

Fig. 6. (a) High resolution cross-sectional TEM images of 1 wt% $Ti_3C_2T_x$-epoxy nanocomposite. (b) TEM reveals intercalation of polymer molecules between MXene flakes at low MXene loading.

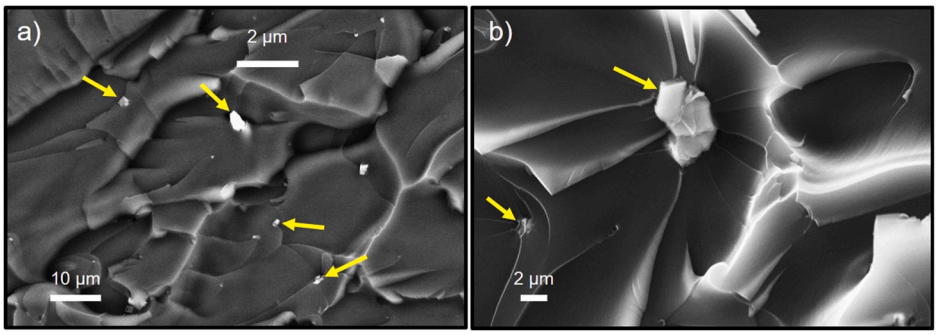

Fig. 7. SEM analysis of 1 wt% $Ti_3C_2T_x$ MXene nanocomposite fracture surface. Backscatter electron (a) and secondary electron (b) images of MXene particles protruding from sample surface at break. Yellow arrows indicate cavities around the edges of MXene particles.

the strong interface model is ~0.2 μm, while the experimental void size is ~4.0 μm (Fig. 7).

4.5. Structural characterization of $Ti_3C_2T_x$-epoxy nanocomposites

The synthesized $Ti_3C_2T_x$-epoxy composite with 1 wt% of the nanofiller component is shown in Fig. 6. MXene flakes show mostly isotropic dispersion throughout the epoxy matrix after curing.

As shown in the TEM images, there is an increase in the spacing between individual $Ti_3C_2T_x$ flakes (black lines) compare to the flake spacing in $Ti_3C_2T_x$ powder, indicating some epoxy molecules were intercalated between the MXene layers. Also, The XRD evidence for epoxy intercalation has been published in our recent research [28].

SEM images (Fig. 7) show samples reinforced with MXene have a rougher fracture surface than neat epoxy which suggests the increased toughness of the nanocomposites, similar to epoxy with graphene nanoplatelets composites [3,4]. SEM Backscatter image of Fig. 7 (b) is placed in Supporting Information as Fig. S7. It has been shown that plastic yielding is one of the major contributions to the fracture toughness improvement of epoxy nanocomposites at a low nanofiller content through the energy dissipation, while the neat epoxy has typical brittle fracture with smooth surface without nanovoid formation [60]. SEM also revealed evidence of the strong bonding along basal plane of MXene flakes and epoxy matrix, where the fracture surface has micrometer-size voids near edges of MXene particles. The flakes act as stress concentrators leading to formation of these voids.

It has been shown that debonding of the nanofiller particles from the matrix and subsequent plastic void growth delays material fracture by dissipation of fracture energy [1,61]. Since analysis of the SEM images shows the evidence of the voids, which we attributed to the plastic void growth, we expect the toughness improvement of these nanocomposites.

5. Conclusion and outlook

In this paper, a computational investigation of epoxy nanocomposites with the integration of two-dimensional $Ti_2C(OH)_2$ and $Ti_3C_2(OH)_2$ MXene-epoxy composites were successfully studied using Density Functional Theory (DFT) and coarse-grained MD simulations. In the DFT simulation, MXenes-epoxy binding energy was largely unchanged by MXene type ($Ti_2C(OH)_2$ or $Ti_3C_2(OH)_2$). Increase of = O and reduction of –OH surface terminations of $Ti_3C_2T_x$ led to the increase in favorable electrostatic interactions and consequently strengthen binding between MXene and epoxy. In the coarse grained MD simulation, it was shown that as the lateral size of the filler sheets increase, then polymer reinforcement improved. The improvement of the Young's modulus of MXene-epoxy nanocomposites is a result of the stress transfer between the matrix system and the nanofiller. However, the MD simulation also confirmed that at higher filler contents, the increase of the modulus is reduced due to filler aggregation. TEM and SEM spectral images were provided to reveal the intercalation of polymer molecules between the MXene flakes at low MXene loading of 1 wt%. It has been shown that the possibilities for MXene nanocomposites are promising reinforcement candidates for epoxies. Hopefully our findings will stimulate opportunities for designing novel materials with increased toughness and impact resistance with the potential of arresting crack propagation for a more damage tolerant material system.

Declaration of competing interest

The authors declare that they have no known competing financial interests or personal relationships that could have appeared to influence the work reported in this paper.

CRediT authorship contribution statement

Yelena Sliozberg: Conceptualization, Methodology, Software, Formal analysis, Investigation, Writing - original draft, Writing - review & editing, Visualization, Supervision, Project administration. **Jan Andzelm:** Conceptualization, Methodology, Software, Formal analysis, Investigation, Visualization, Validation, Writing - original draft, Writing - review & editing. **Christine B. Hatter:** Validation, Visualization, Investigation, Writing - original draft, Writing - review & editing. **Babak Anasori:** Conceptualization, Methodology, Visualization, Investigation, Formal analysis, Writing - review & editing, Supervision. **Yury Gogotsi:** Conceptualization, Methodology, Formal analysis, Supervision, Project administration, Resources, Writing - review & editing. **Asha Hall:** Conceptualization, Supervision, Project administration, Funding acquisition, Writing - review & editing.

Acknowledgments

The authors thank Mark Bundy, Latha Nataraj, Timothy Sirk and Christopher Shumeyko for useful discussions. Calculations were performed using resources at Air Force Research Laboratory and CCDC Army Research Laboratory Supercomputing Resource Centers.

Appendix A. Supplementary data

Supplementary data related to this article can be found at https://doi.org/10.1016/j.compscitech.2020.108124.

References

[1] N. Domun, H. Hadavinia, T. Zhang, T. Sainsbury, G.H. Liaghat, S. Vahid, Improving the fracture toughness and the strength of epoxy using nanomaterials – a review of the current status, Nanoscale 7 (23) (2015) 10294–10329.
[2] L.-C. Tang, Y.-J. Wan, D. Yan, Y.-B. Pei, L. Zhao, Y.-B. Li, L.-B. Wu, J.-X. Jiang, G.-Q. Lai, The effect of graphene dispersion on the mechanical properties of graphene/epoxy composites, Carbon 60 (2013) 16–27.
[3] N. Domun, H. Hadavinia, T. Zhang, G. Liaghat, S. Vahid, C. Spacie, K.R. Paton, T. Sainsbury, Improving the fracture toughness properties of epoxy using graphene nanoplatelets at low filler content, Nanocomposites 3 (3) (2017) 85–96.

[4] M.M. Shokrieh, S.M. Ghoreishi, M. Esmkhani, Z. Zhao, Effects of graphene nanoplatelets and graphene nanosheets on fracture toughness of epoxy nanocomposites, Fatig. Fract. Eng. Mater. Struct. 37 (10) (2014) 1116–1123.

[5] C. Salom, M.G. Prolongo, A. Toribio, A.J. Martínez-Martínez, I.A. de Cárcer, S. G. Prolongo, Mechanical properties and adhesive behavior of epoxy-graphene nanocomposites, Int. J. Adhesion Adhes. 84 (2018) 119–125.

[6] H. Ribeiro, J.P.C. Trigueiro, W.M. Silva, C.F. Woellner, P.S. Owuor, A. Cristian Chipara, M.C. Lopes, C.S. Tiwary, J.J. Pedrotti, R. Villegas Salvatierra, J.M. Tour, N. Chopra, I.N. Odeh, G.G. Silva, P.M. Ajayan, Hybrid MoS2/h-BN nanofillers as synergic heat dissipation and reinforcement additives in epoxy nanocomposites, ACS Appl. Mater. Interfaces 11 (27) (2019) 24485–24492.

[7] D. Galpaya, M. Wang, G. George, N. Motta, E. Waclawik, C. Yan, Preparation of graphene oxide/epoxy nanocomposites with significantly improved mechanical properties, J. Appl. Phys. 116 (5) (2014), 053518.

[8] M. Bhattacharya, Polymer nanocomposites-A comparison between carbon nanotubes, graphene, and clay as nanofillers, Materials 9 (4) (2016) 262.

[9] J. Wei, T. Vo, F. Inam, Epoxy/graphene nanocomposites – processing and properties: a review, RSC Adv. 5 (90) (2015) 73510–73524.

[10] H. Ribeiro, J.P.C. Trigueiro, P.S. Owuor, L.D. Machado, C.F. Woellner, J. J. Pedrotti, Y.M. Jaques, S. Kosolwattana, A. Chipara, W.M. Silva, C.J.R. Silva, D. S. Galvão, N. Chopra, I.N. Odeh, C.S. Tiwary, G.G. Silva, P.M. Ajayan, Hybrid 2D nanostructures for mechanical reinforcement and thermal conductivity enhancement in polymer composites, Compos. Sci. Technol. 159 (2018) 103–110.

[11] S. Chandrasekaran, N. Sato, F. Tölle, R. Mülhaupt, B. Fiedler, K. Schulte, Fracture toughness and failure mechanism of graphene based epoxy composites, Compos. Sci. Technol. 97 (2014) 90–99.

[12] B. Anasori, Y. Gogotsi, 2D Metal Carbides and Nitrides (MXenes) Structure, Properties and Applications Structure, Properties and Applications, 2019.

[13] Y. Zou, L. Fang, T. Chen, M. Sun, C. Lu, Z. Xu, Near-infrared light and solar light activated self-healing epoxy coating having enhanced properties using MXene flakes as multifunctional fillers, Polymers 10 (5) (2018) 474.

[14] R. Liu, W. Li, High-thermal-stability and high-thermal-conductivity $Ti_3C_2T_x$ MXene/poly(vinyl alcohol) (PVA) composites, ACS Omega 3 (3) (2018) 2609–2617.

[15] Z. Ling, C.E. Ren, M.-Q. Zhao, J. Yang, J.M. Giammarco, J. Qiu, M.W. Barsoum, Y. Gogotsi, Flexible and conductive MXene films and nanocomposites with high capacitance, Proc. Natl. Acad. Sci. Unit. States Am. 111 (47) (2014) 16676–16681.

[16] S. Zhao, H.-B. Zhang, J.-Q. Luo, Q.-W. Wang, B. Xu, S. Hong, Z.-Z. Yu, Highly electrically conductive three-dimensional $Ti_3C_2T_x$ MXene/reduced graphene oxide hybrid aerogels with excellent electromagnetic interference shielding performances, ACS Nano 12 (11) (2018) 11193–11202.

[17] H. Zhang, L. Wang, A. Zhou, C. Shen, Y. Dai, F. Liu, J. Chen, P. Li, Q. Hu, Effects of 2-D transition metal carbide Ti_2CT_x on properties of epoxy composites, RSC Adv. 6 (90) (2016) 87341–87352.

[18] B. Anasori, M.R. Lukatskaya, Y. Gogotsi, 2D metal carbides and nitrides (MXenes) for energy storage, Nature Reviews Materials 2 (2017) 16098.

[19] N.K. Chaudhari, H. Jin, B. Kim, D. San Baek, S.H. Joo, K. Lee, MXene: an emerging two-dimensional material for future energy conversion and storage applications, J. Mater. Chem. 5 (47) (2017) 24564–24579.

[20] M. Khazaei, A. Ranjbar, M. Arai, T. Sasaki, S. Yunoki, Electronic properties and applications of MXenes: a theoretical review, J. Mater. Chem. C 5 (10) (2017) 2488–2503.

[21] H.-W. Wang, M. Naguib, K. Page, D.J. Wesolowski, Y. Gogotsi, Resolving the structure of $Ti_3C_2T_x$ MXenes through multilevel structural modeling of the atomic pair distribution function, Chem. Mater. 28 (1) (2016) 349–359.

[22] N. Zhang, Y. Hong, S. Yazdanparast, M. Asle Zaeem, Superior structural, elastic and electronic properties of 2D titanium nitride MXenes over carbide MXenes: a comprehensive first principles study, 2D Mater. 5 (4) (2018), 045004.

[23] M. Barsoum, MAX Phases: Properties of Machinable Ternary Carbides and Nitrides, 2013.

[24] J. Halim, K.M. Cook, M. Naguib, P. Eklund, Y. Gogotsi, J. Rosen, M.W. Barsoum, X-ray photoelectron spectroscopy of select multi-layered transition metal carbides (MXenes), Appl. Surf. Sci. 362 (2016) 406–417.

[25] M.A. Hope, A.C. Forse, K.J. Griffith, M.R. Lukatskaya, M. Ghidiu, Y. Gogotsi, C. P. Grey, NMR reveals the surface functionalisation of Ti_3C_2 MXene, Phys. Chem. Chem. Phys. 18 (7) (2016) 5099–5102.

[26] K. Maleski, V.N. Mochalin, Y. Gogotsi, Dispersions of two-dimensional titanium carbide MXene in organic solvents, Chem. Mater. 29 (4) (2017) 1632–1640.

[27] L. Wang, L. Chen, P. Song, C. Liang, Y. Lu, H. Qiu, Y. Zhang, J. Kong, J. Gu, Fabrication on the annealed $Ti_3C_2T_x$ MXene/Epoxy nanocomposites for electromagnetic interference shielding application, Compos. B Eng. 171 (2019) 111–118.

[28] C.B. Hatter, J. Shah, B. Anasori, Y. Gogotsi, Micromechanical response of two-dimensional transition metal carbonitride (MXene) reinforced epoxy composites, Compos. B Eng. 182 (2020), 107603.

[29] M. Kurtoglu, M. Naguib, Y. Gogotsi, M.W. Barsoum, First principles study of two-dimensional early transition metal carbides, MRS Communications 2 (4) (2012) 133–137.

[30] G. Gao, G. Ding, J. Li, K. Yao, M. Wu, M. Qian, Monolayer MXenes: promising half-metals and spin gapless semiconductors, Nanoscale 8 (16) (2016) 8986–8994.

[31] T. Hu, M. Hu, Z. Li, H. Zhang, C. Zhang, J. Wang, X. Wang, Interlayer coupling in two-dimensional titanium carbide MXenes, Phys. Chem. Chem. Phys. 18 (30) (2016) 20256–20260.

[32] P. Urbankowski, B. Anasori, T. Makaryan, D. Er, S. Kota, P.L. Walsh, M. Zhao, V. B. Shenoy, M.W. Barsoum, Y. Gogotsi, Synthesis of two-dimensional titanium nitride Ti_4N_3 (MXene), Nanoscale 8 (22) (2016) 11385–11391.

[33] I.R. Shein, A.L. Ivanovskii, Graphene-like titanium carbides and nitrides $Ti_{n+1}C_n$, $Ti_{n+1}N_n$ (n=1, 2, and 3) from de-intercalated MAX phases: first-principles probing of their structural, electronic properties and relative stability, Comput. Mater. Sci. 65 (2012) 104–114.

[34] S. Wang, J.-X. Li, Y.-L. Du, C. Cui, First-principles study on structural, electronic and elastic properties of graphene-like hexagonal Ti_2C monolayer, Comput. Mater. Sci. 83 (2014) 290–293.

[35] V.N. Borysiuk, V.N. Mochalin, Y. Gogotsi, Bending rigidity of two-dimensional titanium carbide (MXene) nanoribbons: a molecular dynamics study, Comput. Mater. Sci. 143 (2018) 418–424.

[36] L. Ding, Y. Wei, L. Li, T. Zhang, H. Wang, J. Xue, L.-X. Ding, S. Wang, J. Caro, Y. Gogotsi, MXene molecular sieving membranes for highly efficient gas separation, Nat. Commun. 9 (1) (2018) 155.

[37] B. Delley, An all-electron numerical method for solving the local density functional for polyatomic molecules, J. Chem. Phys. 92 (1) (1990) 508–517.

[38] B. Delley, From molecules to solids with the DMol3 approach, J. Chem. Phys. 113 (18) (2000) 7756–7764.

[39] B. Delley, Fast calculation of electrostatics in crystals and large molecules, J. Phys. Chem. 100 (15) (1996) 6107–6110.

[40] J.P. Perdew, K. Burke, M. Ernzerhof, Generalized gradient approximation made simple, Phys. Rev. Lett. 77 (18) (1996) 3865–3868.

[41] F.L. Hirshfeld, Bonded-atom fragments for describing molecular charge densities, Theor. Chim. Acta 44 (2) (1977) 129–138.

[42] K. Kremer, G.S. Grest, Dynamics of entangled linear polymer melts: A molecular-dynamics simulation, J. Chem. Phys. 92 (8) (1990) 5057–5086.

[43] K. Hagita, H. Morita, M. Doi, H. Takano, Coarse-grained molecular dynamics simulation of filled polymer nanocomposites under uniaxial elongation, Macromolecules 49 (5) (2016) 1972–1983.

[44] C. Ma, T. Ji, C.G. Robertson, R. Rajeshbabu, J. Zhu, Y. Dong, Effect of filler–polymer interface on elastic properties of polymer nanocomposites: a molecular dynamics study, Tire Sci. Technol. 45 (3) (2017) 227–241.

[45] D. Mukherji, C.F. Abrams, Microvoid formation and strain hardening in highly cross-linked polymer networks, Phys. Rev. 78 (5) (2008), 050801.

[46] D. Mukherji, C.F. Abrams, Mechanical behavior of highly cross-linked polymer networks and its links to microscopic structure, Phys. Rev. 79 (6) (2009), 061802.

[47] R. Lovell, A.H. Windle, Conformational analysis of amine-cured epoxy resins, Polymer 32 (12) (1991) 2272–2277.

[48] A. Lipatov, H. Lu, M. Alhabeb, B. Anasori, A. Gruverman, Y. Gogotsi, A. Sinitskii, Elastic properties of 2D $Ti_3C_2T_x$ MXene monolayers and bilayers, Science Advances 4 (6) (2018), eaat0491.

[49] T.D. Nguyen, C.L. Phillips, J.A. Anderson, S.C. Glotzer, Rigid body constraints realized in massively-parallel molecular dynamics on graphics processing units, Comput. Phys. Commun. 182 (11) (2011) 2307–2313.

[50] S. Plimpton, Fast parallel algorithms for short-range molecular dynamics, J. Comput. Phys. 117 (1) (1995) 1–19.

[51] M. Alhabeb, K. Maleski, B. Anasori, P. Lelyukh, L. Clark, S. Sin, Y. Gogotsi, Guidelines for synthesis and processing of two-dimensional titanium carbide ($Ti_3C_2T_x$ MXene), Chem. Mater. 29 (18) (2017) 7633–7644.

[52] J.L. Hart, K. Hantanasirisakul, A.C. Lang, B. Anasori, D. Pinto, Y. Pivak, J.T. van Omme, S.J. May, Y. Gogotsi, M.L. Taheri, Control of MXenes' electronic properties through termination and intercalation, Nat. Commun. 10 (1) (2019) 522.

[53] M. Seredych, C.E. Shuck, D. Pinto, M. Alhabeb, E. Precetti, G. Deysher, B. Anasori, N. Kurra, Y. Gogotsi, High-temperature behavior and surface chemistry of carbide MXenes studied by thermal analysis, Chem. Mater. 31 (9) (2019) 3324–3332.

[54] L.M. Hall, K.S. Schweizer, Structure, scattering patterns and phase behavior of polymer nanocomposites with nonspherical fillers, Soft Matter 6 (5) (2010) 1015–1025.

[55] Y.R. Sliozberg, T.L. Chantawansri, J.L. Lenhart, J.W. Andzelm, Structural and mechanical properties of advanced polymer gels with rigid side-chains using coarse-grained molecular dynamics, Polymer 55 (20) (2014) 5266–5275.

[56] D.G. Papageorgiou, I.A. Kinloch, R.J. Young, Mechanical properties of graphene and graphene-based nanocomposites, Prog. Mater. Sci. 90 (2017) 75–127.

[57] P. May, U. Khan, A. O'Neill, J.N. Coleman, Approaching the theoretical limit for reinforcing polymers with graphene, J. Mater. Chem. 22 (4) (2012) 1278–1282.

[58] I. Greenfeld, H.D. Wagner, Nanocomposite toughness, strength and stiffness: role of filler geometry, Nanocomposites 1 (1) (2015) 3–17.

[59] J.B. Knoll, B.T. Riecken, N. Kosmann, S. Chandrasekaran, K. Schulte, B. Fiedler, The effect of carbon nanoparticles on the fatigue performance of carbon fibre reinforced epoxy, Compos. Appl. Sci. Manuf. 67 (2014) 233–240.

[60] M. Salviato, M. Zappalorto, M. Quaresimin, Plastic yielding around nanovoids, Procedia Engineering 10 (2011) 3316–3321.

[61] A.J. Kinloch, A.C. Taylor, The mechanical properties and fracture behaviour of epoxy-inorganic micro- and nano-composites, J. Mater. Sci. 41 (11) (2006) 3271–3297.